Submitted
to ApJ

Draft

The Circumstellar Medium of Cassiopeia A Inferred from the Outer Ejecta Knot Properties

Una Hwang[1] & J. Martin Laming[2]

ABSTRACT

We investigate the effect of the circumstellar medium density profile on the X-ray emission from outer ejecta knots in the Cassiopeia A supernova remnant using the 1 Ms Chandra observation. The spectra of a number of radial series of ejecta knots at various positions around the remnant are analyzed using techniques similar to those devised in previous papers. We can obtain a reasonable match to our data for a circumstellar density profile proportional to r^{-2} as would arise from the steady dense wind of a red supergiant, but the agreement is improved if we introduce a central cavity around the progenitor into our models. Such a profile might arise if the progenitor emitted a fast tenuous stellar wind for a short period immediately prior to explosion. We review other lines of evidence supporting this conclusion. The spectra also indicate the widespread presence of Fe-enriched plasma that was presumably formed by complete Si burning during the explosion, possibly via alpha-rich freezeout. This component is typically associated with hotter and more highly ionized gas than the bulk of the O- and Si-rich ejecta.

1. Introduction

More than three hundred years after the event, the optical supernova spectrum of the explosion that formed the Cassiopeia A supernova remnant (SNR) has been observed in a scattered light echo and establishes that the supernova was of type IIb (Krause et al. 2008).

---

[1]NASA/GSFC Code 662, Greenbelt MD 20771

Una.Hwang-1@nasa.gov

[2]Space Science Division, Naval Research Laboratory, Code 7674L, Washington DC 20375

The spectrum strongly resembles that of the IIb prototype SN 1993J at maximum, with broad Hα and weak He lines indicating that the red supergiant exploded with a thin layer of the H envelope remaining outside the He core. The IIb supernovae form a transition between the Type II explosions of massive stars that retain a substantial H layer and the Type Ib explosions of stars that have entirely lost their H envelope in a presupernova stellar wind; the late-time spectra of IIb events transform to resemble those of Ib's. For Cas A, the IIb classification is consistent with the presence of a number of fast ejecta knots showing optical H emission (e.g., Chevalier & Oishi 2003).

Cas A's echo spectrum is distinguished from those of normal Type II supernovae by the presence of broad absorption lines in the spectrum due to the Doppler broadening of the rapidly expanding ejecta and the absence of prominent unresolved lines. This led Krause et al. (2008) to suggest that dense circumstellar material did not reach to the surface of the Cas A progenitor, but rather that the progenitor created a small bubble in the circumstellar medium by emitting a fast stellar wind prior to explosion. The extent of such a wind is limited by the presence of prominent "jet" structures in Cas A today, which are indeed demonstrated to be associated with asymmetries in the explosion (Laming et al. 2006). In the most extreme cases, emerging jets could be destroyed by an encounter with a swept-up mass shell on the periphery of a bubble periphery. To avoid destruction of the jets, the duration of a pre-explosion fast wind in the Cas A progenitor is limited by hydrodynamical simulations to less than about 2000-2500 years (Schure et al. 2008). This places the maximum radius for a bubble at 0.3-0.35 pc.

There have also been prior suggestions for the presence of a circumstellar bubble. A short ($\sim 10^4$ yr) Wolf-Rayet phase has been suggested for Cas A by Garcia-Segura et al. (1996) to provide consistency for the results of their simulations of the circumstellar structure with the low velocities and small radii measured for the optically emitting quasi-stationary flocculi (QSFs). In the work of Laming & Hwang (2003), radial series of X-ray emitting ejecta knots in Cas A were examined in the context of the one-dimensional hydrodynamics of ejecta, assuming an ejecta density profile with a power-law envelope and a constant density core evolving into a $\rho \propto r^{-2}$ circumstellar environment. The inconsistency in this model of blast wave velocities slightly higher and radii lower than those measured directly by DeLaney & Rudnick (2003), can also be resolved if the remnant evolved for a time in a small circumstellar bubble such as might be formed during a short Wolf-Rayet phase.

In this paper we explore these ideas further using the 1 Ms X-ray observation of Cas A obtained by Chandra (Hwang et al. 2004). As in previous work by Laming & Hwang (2003), Hwang & Laming (2003) and Laming et al. (2006), we interpret the ejecta knots and filaments that dominate the X-ray appearance of Cas A as "knots" of distinctive ejecta composition

rather than as knots of substantially higher density, with the rationale that highly overdense knots will be efficiently disrupted by hydrodynamical instabilities. Here we will examine the spectra of several radial series of ejecta knots in the context of hydrodynamical models that incorporate a small circumstellar bubble within the red supergiant wind.

2. X-ray Spectral Analysis

2.1. Introduction

For the X-ray spectral study, we use a 1 Ms observation with the backside-illuminated S3 chip of the Advanced CCD Imaging Spectrometer (ACIS) on the Chandra Observatory (Hwang et al. 2004). These data were obtained in 2004 in nine observation segments, all but one of which occurred over a period of three consecutive weeks. The data extraction procedure essentially follows that described in Laming et al. (2006), with updated calibrations (CIAO-4.0, CALDB-3.4) applied to the data. The data were cleaned to exclude non-standard event grades, bad pixels, and time intervals with high background levels to yield 980 ks of exposure time. The data were also corrected for the time-dependent gain of the detector, but could not be corrected for charge-transfer inefficiency given that the events were characterized on board the satellite before telemetry (i.e., the data were obtained in Chandra GRADED mode).

A number of approximately radial "series" of several knots each were chosen to sample the spectra at a range of azimuthal locations as shown in Figure 1. The size of the spectral regions varied from $1.5''$ to $6''$ on a side, with most averaging 2-3''. The spectra are of very high quality, typically containing from a few to several tens of thousands of counts. A single spectrum and corresponding spectral calibration files were calculated for each region by weighting the individual contributions from each observation segment according to the relative exposure time, and then combining them. The spectral background was taken from a single set of off-source regions on the detector.

We consider ejecta regions only. We then assume that the continuum comes mainly from ionized O and heavier elements, and accordingly set the abundances of the lighter elements to zero. It is also possible to model the spectra with a light element continuum including H and He. The assumption of which light elements provide the continuum does affect inferences about electron densities and masses in the knot. While some H and He is certainly present in the remnant given its Type IIb classification, the Cas A progenitor exploded at only 4 $M_\odot$ (Young et al. 2006), so it should have lost most of the gas in its outer layers. Moreover, the regions we select are taken to be enriched in heavy elements by instabilities during the

explosion.

The basic spectral model we use is a single-temperature nonequilibrium ionization (NEI) plasma modified by interstellar absorption. This model has a single average ionization age (defined by the product of electron density and the time since shock passage). Given the known, significant bulk velocities of the ejecta-dominated gas (e.g., Markert et al. 1983), we also allow for additional Gaussian broadening above the detector response, and a red- or blue-shift for the plasma. We thereby obtain the average electron temperature and ionization age, the element abundances, and a measure of the line-of-sight velocity.

Spectral complexity is seen, however, at a number of levels. First, plane-parallel shock models, which include a range of ionization ages from zero up to a fitted maximum, were generally more successful with our data than NEI models, mainly because they are better able to characterize the shape of the Fe L blend. While plane-parallel shock spectral models do not increase the number of fitted parameters, they are more difficult to interpret in the context of the hydrodynamical models discussed in section 3. For that reason, we favor the NEI models for this discussion. The actual fitted parameters are quite comparable, in the sense that the temperatures are similar and the maximum ionization age in the plane-parallel shock model generally turns out to be about twice the average ionization age in the NEI models used here.

Second, most of the spectra show a Fe K blend which is left unaccounted for by the single-component NEI models. Even single-component plane-parallel shock models are successful in this respect in only a very limited number of cases, typically those where the Fe K blend is especially prominent. Such spectra usually also feature a prominent Fe L blend, and high ratios of the Si Ly α to He α emission (for example, see knots B8 and B11 in Figure 2). In the remaining majority of cases where single component NEI and plane-parallel shock models are both inadequate, the addition of a second spectral component including *only* Fe and Ni does provide significantly improved fits.

Our final spectral model is thus a two-component NEI model, with one component corresponding to O-rich ejecta including all the abundant elements heavier than O, and the second including only Fe and Ni. The redshift of the Fe component was fixed at 0 in order to better constrain the other parameters. In most cases, this second component did act to fill in the Fe K blend. In just a few instances, it preferred instead to improve the shape of the Fe L blend; those cases, however, might be better handled with a range of ionization ages. Throughout, the O-rich ejecta component remains dominant, and its properties are generally not much changed from the single NEI case, though there are a few exceptions. Generally, these reduce the high temperatures of the main ejecta component for some of the knots (mostly in the B and E series), although there were also a few instances where the

ejecta temperature increased. We discuss the Fe components a little further in the following subsection.

The fitted temperatures for the main ejecta component for these knots are typically 1-2 keV, and the average ionization ages are most often in the low- to mid- 10^{11} cm^{-3}s range. Significant differences are seen amongst the various sets, with somewhat higher temperatures measured for certain knots, especially in series A, D, J, L, M, and N. The knots in the western region of the remnant tend to have higher fitted temperatures on the whole. The column density varies significantly across the remnant, as has been frequently noted in previous observations (e.g., Eriksen et al. 2009, Keohane et al. 1996, Troland et al. 1985), with the highest values in this set seen in the west (i.e., series J and K), where a molecular cloud is known to be interacting with and obscuring the remnant.

We give all the two component NEI fit results in Table 1, but rather than showing the spectra for all hundred or so knots considered here, we do so only for selected knots from two particular radial series (B and N) in Figure 2. The knots in series B generally have a strong Fe K blend and show a strong evolution in ionization age that can be traced by the Si Ly α/He α ratio. The knots in series N are representative of those that have weaker Fe K emission and more uniform spectral properties. For these and all other sets of knots, we plot the fitted temperatures and ionization ages of the knots in Figure 3, together with the models that will be described shortly in section 3.

2.2. Fe plasma component

As noted above, no single-component NEI models were able to reproduce the entire spectrum of any knot showing an Fe K blend, whereas two such components did in most cases provide significantly improved fits to the spectrum, including the Fe K emission. While the Fe component is not the focus of this study and we do not undertake a detailed interpretation of it here, we do note that the fitted temperatures Fe component are generally rather high at above 2 keV, and that ionization ages are often, though not always, higher than the main ejecta component–generally a few to several 10^{11} cm^{-3}s.

Aside from the obvious indication of widespread spectral complexity even on 2-3″ angular scales, it appears that the spectra of many of the knots do require an additional emission component that is consistent with pure Fe or very high enrichment in Fe. In their early Chandra assay of ejecta knots in Cas A, Hughes et al. (2000) note that strong Fe K emission accompanying strong Si emission likely indicates the presence of additional Fe ejecta beyond the relatively low Fe yield produced by incomplete Si burning. Presumably, this additional

Fe is nearly pure Fe from complete Si burning with or without alpha-rich freezeout. The results of Willingale et al. (2002) suggest that certain lines of sight should indeed include a juxtaposition of ejecta of various compositions and velocities. Our results support the idea that an Fe-enriched ejecta component is widespread throughout the remnant in the regions that we sampled.

Second, this Fe enriched plasma tends to be hotter and is probably more highly ionized than the main ejecta component that includes O, Si, and other elements. In the models that we will describe in the next section, these ionization ages correspond to an ejecta Lagrange mass coordinate of ~ 0.4, where 0 corresponds to the outermost layers of ejecta and 1 to the mass cut at the presumed neutron star. Thus for 2 $M_\odot$ ejecta mass, the Fe is at a significant distance of approximately 1.2 $M_\odot$ from the mass cut. In the cases where highly enriched Fe plasma seems to have been well-mixed with other plasma (i.e., those knots where a simple plane-parallel shock component could describe all the emission), there appears to be a tendency for even higher degrees of ionization. Marked evolution in ionization age can be seen the radial series located in the eastern region of the remnant, e.g., series B, C, D, and E. Such high ionization ages are not commonly seen in Cas A, and as it turns out, the eastern region in the remnant is where a high degree of Fe enrichment is most clearly observed (Hwang & Laming 2003).

We defer a comprehensive study of the properties of this Fe emission for a forthcoming paper. For the time being, we restrict ourselves to the observation that these spectra clearly show a widespread contribution from plasma enriched in Fe that have distinct plasma properties from the other ejecta plasma.

2.3. Forward shock and nonthermal emission

Aside from the spectral complexity due to multiple ejecta components, it is also possible that there will be some significant emission projected from the forward shock, even in these ejecta-dominated regions. Recent work has shown that the forward shock emission in young remnants is more strongly dominated by nonthermal than thermal processes. Moreover, in Cas A, even the interior regions of the remnant have been shown to be associated with hard nonthermal X-ray emission (Bleeker et al. 2001; Helder & Vink 2008). We assessed the location of our ejecta knots on the 8-15 keV hard continuum image obtained from a 2000 observation with the PN detector on XMM-Newton (obsid 0097610801, which is shown here in Figure 1, and is similar to that in Bleeker et al. 2001), as well as the 4-6 keV Chandra continuum image. Contamination from nonthermal emission is more likely in the west, where it is strongest, but the Chandra images show that the hard emission is distributed in highly

filamentary features throughout the remnant. Precise coincidences between our chosen region and the hard X-ray emission are not common, but given that the 4-6 keV emission is variable with a timescale of order a year (Uchiyama & Aharonian 2008; Patnaude & Fesen 2007), one might expect the 8-15 keV continuum to be similarly variable if it is produced by the same mechanism.

All of the knots presented here are true ejecta-dominated features, but the presence of a nonthermal component could in principle significantly affect the inferred temperatures and abundances for the ejecta knots. The addition of a power-law component certainly does change the fitted temperature of the thermal ejecta component in some knots with particularly strong continuum that we have not included here. Their initially high fitted temperatures of 2-3 keV were reduced significantly with the introduction of a power-law continuum to the model, while the uncertainties in the temperatures increased significantly. In virtually all the cases considered here, however, the line emission from the ejecta is strongly dominant so that the fits are driven more strongly by the ejecta line emission than by the high-energy continuum. In the few cases where there is a clear deficit in the continuum at high energies for single component NEI models—for example in knots H5 and H6—we generally found that fitting a power-law component of the expected ∼2.7 slope (rather than a second NEI component) did little to change the fitted temperature for the main ejecta component. The fact that higher plasma temperatures are observed in region in the west where the hard emission is stronger is very interesting, however, in that it may have implications for the nature of this emission, as regards to whether it is produced by synchrotron emission or nonthermal bremsstrahlung. We discuss this a little further in section 4.2.

3. Modeling and Interpretation

We model the spectra of the outer knots of Cas A using the approximations and methods developed in Laming & Hwang (2003) and Hwang & Laming (2003), extended to deal with the case of expansion into a stellar wind incorporating a "bubble" around the supernova. This is presumed to arise from a short spell of fast tenuous stellar wind just prior to the supernova explosion. In our treatment, a zero density spherical bubble is centered on the supernova, and the density obeys $\rho \propto 1/r^s$ outside the bubble. We do not include the effect of a swept-up shell of circumstellar material at the bubble periphery, but merely consider a pure stellar wind density profile with a cavity in the center.

We take the model in Laming & Hwang (2003) for a $1/r^s$ (with $s = 2$) circumstellar density profile with no bubble as a "fiducial" model, and approximate that the forward shock velocity in the model including the bubble should be the same as that in the fiducial model

when the same mass of circumstellar plasma has been swept up. Then the forward shock radii in the fiducial case, r_{b0}, and in the real case, r_b, are related by

$$r_{b0}^3 = r_b^3 - r_b^s r_{bub}^{3-s} \tag{1}$$

where r_{bub} is the bubble radius. (We reference all quantities for the fiducial model with a 0 subscript.) The ejecta are treated as having a constant density core, surrounded by an outer envelope with density $\rho \propto 1/r^n$. Throughout this work we take $n = 10$, following the treatment of Matzner & McKee (1999) for blast wave propagation through the outer layers of a highly stripped progenitor. Solutions for forward and reverse shock motion in the core and envelope phases (i.e. when the reverse shock is propagating through the ejecta core or envelope) can be found separately and coupled at the transition time. For $s > 0$, Laming & Hwang (2003) adopted a simpler approximation of extending the envelope blast wave trajectory into the core phase, and coupling it directly to the appropriate form of the blast wave in the Sedov-Taylor limit, which occurs at a time t_{conn} (equations A10 - A12 in Laming & Hwang 2003). We adapt this procedure to the case with a bubble as follows.

While the ejecta envelope is still interacting with the bubble wall, the forward shock velocity is

$$v_b(t) = \left(\frac{n-3}{n-s}\right)\left(\frac{r_b - r_{bub}}{t - t_{bub}}\right) = v_{b0}(t) = \left(\frac{n-3}{n-s}\right)\frac{r_{b0}}{t_0}, \tag{2}$$

giving

$$t = \frac{t_0}{r_{b0}}(r_b - r_{bub}) + t_{bub} \tag{3}$$

where t_{bub} is taken to be the time at which the forward shock that is driven into the stellar wind exterior to the bubble has been accelerated to v_{core}, which is the expansion velocity of the ejecta at the core-envelope boundary. This time is calculated from equation 3.20 for the forward shock radius in Chevalier & Liang (1989), by taking the time derivative and equating it to $v_{core} = \sqrt{10(n-5)/3/(n-3)}$ (in units of $7090\sqrt{E_{51}/M_{ej}}$ km s^{-1} where E_{51} is the explosion energy in 10^{51} ergs and M_{ej} is the ejecta mass in solar masses) to give

$$t_{bub} = \left[\frac{2\rho v_b^2 r_{bub}^{n-2}(n-4)}{(n-3)KA}\right]^{1/(n-5)}. \tag{4}$$

Here $K = 0.8\left[1 + 1.25/(n-5)\right]^{(n-2)/3}$ for $\gamma = 5/3$ gas, and A is defined by the ejecta envelope density $\rho_e = Ar^{-n}t^{n-3}$ to give $A = (3/4\pi)M_{ej}v_{core}^{n-3}(n-3)/n$.

The initial positions of the contact discontinuity and reverse shock in the bubble model, r_{cd} and r_r respectively, are estimated as follows. When the same mass of circumstellar material has been swept up in both the fiducial and bubble models, the ratio of the densities

of shocked circumstellar gas is

$$\frac{\rho_0}{\rho} = \frac{\int_0^{r_b} \left(n_0 r_{b0}^s/r^s\right) 4\pi r^2 dr / \left(4\pi r_{b0}^3/3\right)}{\int_{r_{bub}}^{r_b} \left(n_0 r_{b0}^s/r^s\right) 4\pi r^2 dr / \left(4\pi \left(r_{b0}^3 - r_{bub}^3\right)/3\right)} = \frac{r_b^3 - r_{bub}^3}{r_b^3 - r_b^s r_{bub}^{3-s}}. \tag{5}$$

Equating this to $\left(r_b^3 - r_{cd}^3\right) / \left(r_{b0}^3 - r_{cd0}^3\right)$ yields

$$r_{cd} = \left[r_b^3 - \left(r_{b0}^3 - r_{cd0}^3\right) \frac{r_b^3 - r_{bub}^3}{r_b^3 - r_b^s r_{bub}^{3-s}} \right]^{1/3}. \tag{6}$$

The reverse shock position during the envelope phase is given by

$$r_r = \frac{r_b - r_{bub}}{l_{ED}} + v_{core} t_{bub}. \tag{7}$$

We use this expression in the core phase also, corrected at late times to ensure that the reverse shock remains behind the contact discontinuity.

Within this framework of analytic hydrodynamics, we compute the evolution of the postshock ionization balance and electron and ion temperatures, using the prescriptions in Appendix B of Laming & Hwang (2003). A summary of SNR evolution models with various bubble sizes is given in Table 2. The age of Cas A is constrained by observations of optical ejecta knots, with the earliest possible explosion date assuming undecelerated ejecta knots being A.D. 1671.3±0.9 (Thorstensen & Fesen 2001), and that taking deceleration into account being A.D. 1681 ±19 (Fesen et al. 2006). Given these age constraints, models with a bubble size of 0.2 - 0.3 pm appear to be the most likely. Smaller bubbles require explosion dates earlier than 1671 to allow the blast wave to expand to the observed radius at its observed velocity near 5000 km s^{-1}. Larger bubbles correspondingly require later explosion dates, but are convincingly ruled out by the work of Schure et al. (2008).

4. Results and Discussion

4.1. Introduction

We present models for a variety of elemental abundances as given in Table 3, which are chosen to illustrate the range of compositions encountered in our study. While higher concentrations of heavy elements increase the radiative losses and allow faster cooling, this is only important once the plasma electron temperature is well below 10^7 K, which is outside the range of temperatures that we study here. Measured temperatures and ionization ages for knots in all the radial series are shown in Figure 3 against models including bubbles of radius 0, 0.2, and 0.3 pc calculated with the M4 set of abundances from Table 3. The

effect of the varying element abundance on the predicted temperatures and ionization ages is illustrated in the final panels of the same figure, where we also show the N series with models for the K10 and C10 set of abundances, which bracket the range of abundances considered in the models. The model curves are seen to be generally similar.

4.2. Limits on Bubble Size

Compared to models for evolution into a pure circumstellar wind, the main important effect of including a bubble is to increase the temperature of the ejecta knots. This occurs because the knots are reverse-shocked to approximately the same temperature in both cases, but at a larger reverse shock radius in the bubble case. Hence the shocked plasma undergoes less cooling by adiabatic expansion as it evolves to the current size and age. This effect is seen most clearly in the series of knots taken from the eastern side of the remnant, in Figure 3. Series B, C and D are seen to favor bubble models over a pure $1/r^2$ density profile. Series A and F are ambiguous while series G appears to favor a pure stellar wind profile.

The presence of a bubble improves agreement between the predicted mass of radiatively cooled gas and that observed. The optical emission of Cas A is completely accounted for by the emission from dense knots of plasma (Hammell & Fesen 2008), leaving no room for emission from plasma that was initially heated by the shock to X-ray emitting temperatures and has since cooled by radiation to lower optical (or infra-red) emitting temperatures. By contrast, Laming & Hwang (2003) estimate that about $0.6 M_\odot$ of radiatively cooled gas should be present in pure O ejecta with an outer ejecta density profile with slope $n = 10$ expanding into an unmodified stellar wind. Pure He ejecta reduces this radiatively cooled mass to $0.25 M_\odot$, but that is still significantly more mass than is indicated by the observations. Allowing the remnant to expand into a bubble before encountering the stellar wind profile reduces the density and hence the amount of energy lost to radiation. In pure O, the thermal instability disappears in models with a bubble radius of 0.24 pc, and in pure He at 0.09 pc.

On the western side of the remnant, many of the knots (e.g. series L, M, N) show temperatures even higher than can be accounted for by the bubble models we have considered. As already noted, the XMM map of emission in the 8-15 keV band (Bleeker et al. 2001, and Figure 1) does show high intensity close to series J, K, L, M, and N on the west limb, and close to D and E on the east limb.

The hard X-ray emission in Cas A appears to be largely associated with ejecta, even though its origin remains under debate, with Laming (2001a) and Laming (2001b) arguing for nonthermal bremsstrahlung based on X-ray emission over a broad energy range, and

other authors (Helder & Vink 2008) concentrating mainly on the 4-6 keV band and arguing for synchrotron emission. Nonthermal bremsstrahlung from nonrelativistic suprathermal electrons as suggested by Laming (2001a) and Laming (2001b) is expected to naturally heat the ambient thermal electrons by Coulomb collisions. In fact this Coulomb heating represents a much bigger energy sink for the suprathermal population than does the radiated bremsstrahlung, as discussed in detail for the expanding plasma of Cas A by Laming (2001b). By contrast, relativistic electrons emitting synchrotron radiation do not heat the ambient plasma so efficiently. In order to have electrons accelerated as cosmic rays at all, however, electron heating must occur at the shock in order to provide an injection mechanism. Our models assume no shock electron heating beyond a simple application of the jump conditions. For both cases, we might reasonably expect to see higher electron temperatures than predicted, but the correspondence between accelerated electrons and plasma heating in the synchrotron case is less direct than in the nonthermal bremsstrahlung case.

4.3. Implications for Progenitor

It is now established that Cas A underwent a Type IIb supernova event and exploded with at least a thin layer of H intact. The echo spectrum presented by Krause et al. (2008) resembles that of the IIb prototype SN 1993J, which is inferred to have occured in a binary system with a massive progenitor of 15-20 $M_\odot$ that evolved to a 3-6 $M_\odot$ He core. Binary scenarios are also implicated for other IIb events, such as SN 2008ax (Crockett et al. 2008).

In terms of enabling a short Wolf-Rayet phase that would create the required circumstellar bubble, a binary scenario may be more promising than those for a single star. Woosley et al. (1993) model a sample of single massive stars with masses in the range 35 - 85 $M_\odot$. Only stars with initial masses around 60 $M_\odot$ are able to expel enough material to approach $\sim 4 M_\odot$ upon explosion, but such an explosion would not be a Type IIb event, since all the H would have been lost during the pre-supernova evolution. Eldridge & Tout (2004) give similar conclusions. Young et al. (2006) consider in more detail both single and binary progenitor models specifically for Cas A, with progenitors in the mass range 16-40 $M_\odot$. In terms of being able to reproduce the small ejecta masses at explosion, along with other observables of the Cas A SNR, 16 or 23 $M_\odot$ stars with binary companions are strongly favored. Single stars of 23 or 40 $M_\odot$ have final ejecta masses that are too large, and need explosions that are significantly more energetic than the accepted 2×10^{51} ergs if they are to avoid producing a black hole remnant. The final parameters inferred for Cas A by Young et al. (2006) are similar to those cited above for SN 1993J, at 15-25 $M_\odot$ evolving to 4 $M_\odot$ at explosion.

Binary progenitor systems may indeed be widespread for the core-collapse supernovae,

given that a better match can be obtained to observed stellar population and core-collapse supernova rates when binary interactions are taken into account (e.g., Eldridge et al. 2008). Relevant to the formation of a compact circumstellar bubble, a binary interaction makes a Wolf-Rayet phase possible for lower mass stars, and allows the Wolf-Rayet phase for these stars to be short enough that only a compact bubble would be formed.

A further constraint is provided by light echo observations in the infrared. Aside from the light echo spectrum studied by Krause et al. (2008), light echoes from Cas A have also been observed by Rest et al. (2008), and in the infra-red by Dwek & Arendt (2998). This last observation does not represent the direct scattering of optical light from the explosion, but rather the heating of dust by EUV-UV radiation associated with shock breakout, followed by reradiation at infra-red wavelengths. The infra-red echoes are located externally to Cas A, and so the illuminating EUV-UV radiation must have traveled through the RSG wind from the interior. Dwek & Arendt (2998) consider cases of dust irradiation by EUV photons from shock breakout under conditions where the RSG wind is optically thin (a maximum H column of 1.5×10^{20} cm^{-2}). The hydrogen column density in the wind is approximately $1.4 \times 10^{38}/r_{bub}$ where r_{bub} is the radius of the inner edge of the RSG wind, which is the bubble radius. For the H column of Dwek & Arendt (2998), r_{bub} is ~ 0.3 pc, which is entirely consistent with our previous discussion. At higher H column densities, the required shock breakout luminosities exceed $10^{12} L_{\odot}$. These are higher than those modeled by Blinnikov et al. (2000) for the case of SN 1987A, so while they are not ruled out, they must be considered unlikely. Of course radiation from the SN event is likely to completely ionize the surrounding CSM, especially as there is no neutral material ahead of the forward shock at 2.5 pc radius. Our concern here, however, is with the shock breakout radiation, which represents a small fraction of the total radiation in photons from the supernova event, and which is most likely emitted *before* such photoionization takes place.

Supernova shock breakout has also been observed *in real time* by *GALEX* (Schawinski et al. 2008; Gezari et al. 2008). In each case, the rise in UV emission as the shock emerges through the photosphere of the RSG progenitor was observed, although the two sets of authors have slightly different interpretations. By way of contrast, there are also claims of observations of shock breakout in explosions with more stripped progenitors that are more similar to Cas A. For SN 2008D, observed in X-rays by *Swift*, the inferred photospheric radius is $> 6 \times 10^{12}$cm, (Soderberg et al. 2008; Chevalier & Fransson 2008), which is larger than the typical radii, $\sim 10^{11}$ cm, of Wolf-Rayet stars. This makes the presence of a dense stellar wind close to the stellar surface likely, with no significant "bubble". Chevalier & Fransson (2008) also consider the optical observations of shock breakout in SN 1987A, SN 1999ex, and SN 2008D, in all cases finding radii of order $\sim 10^{14}$ cm. Such a distance is significantly larger than the likely stellar radius, but is also substantially smaller than the putative bubble

radius for Cas A. It appears that in all these cases, dense wind exists much closer to the progenitor at the time of explosion than was the case for Cas A. Claims of shock breakout in SN 2006aj are more controversial (e.g. Soderberg et al. 2006).

It is also worthwhile to consider the similarities and differences between Cas A and the long-soft GRBs that are associated with core-collapse supernovae. While Cas A was not likely associated with a "classical" gamma-ray burst (Laming et al. 2006), it might have some relation to lower energy GRBs or X-ray flashes (XRFs). Its progenitor clearly underwent the same kind of substantial mass loss that allows the relativistic jet in GRBs to penetrate the stellar layers at explosion and generate the burst. Further similarities include the presence of Cas A's ejecta jets, and an inferred mass at explosion and explosion energy that are in line with those inferred for the less energetic examples of long GRBs. In particular, the explosion energy and progenitor mass at explosion determined by Laming & Hwang (2003) for Cas A are nearly identical to the values of 2×10^{51} ergs and 2 $M_\odot$, respectively, inferred for GRB/XRF 060218/SN 2006aj (Mazzali et al. 2006), though this Type Ic event was even more stripped by stellar wind mass loss than was Cas A. Similar mass and explosion energies have also been inferred for other examples of unusual Ib/Ic explosions that are not associated with GRBs, such as SN 2008d (ejecta mass 3-5 $M_\odot$, explosion energy $2 - 4 \times 10^{51}$ erg, Soderberg et al. 2008) and SN 2005bf (ejecta mass 8.3 $M_\odot$, explosion energy 2×10^{51} erg, Folatelli et al. 2006).

5. Conclusion

In this work, we have explored a simplified one-dimensional circumstellar environment that nevertheless provides a workable model for Cas A. We have presented several lines of evidence to suggest that Cas A evolved into a small circumstellar bubble of approximately 0.2-0.3 pc radius located inside the circumstellar wind. Aside from allowing higher temperatures for the ejecta knots that are more consistent with the results of spectral fits to X-ray data, the presence of a bubble provides better agreement with the dynamics and radii of the shocks, as noted previously, and reduces the mass of radiatively-cooled ejecta to be in better agreement with the optical observations. Further support for the the likely presence of circumstellar bubbles in Cas A include its likely binary progenitor, and estimates for the supernova shock breakout luminosity and its processing in the surrounding environment.

One puzzle that remains here involves the presence of nonthermal emission superposed with the ejecta knot spectra, and the extent to which these might affect inferred temperatures for the ejecta knots. The temperatures seen in the spectra are systematically higher exactly where the nonthermal emission is most prominent, but a more sophisticated and larger-scale

treatment of the nonthermal emission may be required to do assess this properly, as it is difficult to constrain the low level of nonthermal emission in these ejecta spectra.

Finally, the ejecta spectra studied here clearly show the presence of a component that is most simply described by plasma highly enriched in Fe. This component occurs in knots at locations throughout Cas A, and appears to tend toward higher temperatures and ionization ages. The presence of highly pure Fe implies explosive Si burning, possibly by alpha-rich freezeout. Highly pure Fe was identified by Chandra in the southeast (Hwang & Laming 2003), but the present study indicates that such pure Fe may be present on a large scale, superposed with ejecta of a more normal composition. A more comprehensive study of the Fe ejecta in Cas A is the subject of a subsequent study.

REFERENCES

Bleeker, J. A. M., Willingale, R., van der Heyden, K., Dennerl, K., Kaastra, J. S., Aschenbach, B., & Vink, J. 2001, A&A, 365, L225

Blinnikov, S. 2000, ApJ, 532, 1132

Campana, S., et al. 2006, Nature, 442, 1008

Chevalier, R. A., & Liang, E. P. 1989, ApJ, 344, 332

Chevalier, R. A., & Oishi, J. 2003, ApJ, 593, L23

Chevalier, R. A., & Fransson, C. 2008, ApJ, 683, L135

Crockett, R. M., et al. 2008, MNRAS, 391, L5

DeLaney, T. A., & Rudnick, L. 2003, ApJ, 589, 818

Dwarkadas, V. V. 2005, ApJ, 630, 892

Dwarkadas, V. V. 2007, ApJ, 667, 226

Dwek, E., & Arendt, R. G. 2008, ApJ, 685, 976

Eldridge, J. J., & Tout, C. A. 2004, MNRAS, 353, 87

Eldridge, J. J., Izzard, R. G., & Tout, C. A., 2008, MNRAS, 384, 1109

Eriksen, K. A., Arnett, D., McCarthy, D. Q., & Young, P. 2009, ApJ in press, arXiv:0902.4029

Fesen, R. A., Hammell, M. C., Morse, J. Chevalier, R. A., Borkowski, K. J., Dopita, M. A., Gerardy, C. L., Lawrence, S. S., Raymond, J. C., & van den Bergh, S. 2006, ApJ, 645, 283

Folatelli, G., et al. 2006, ApJ, 641, 1039

Galama, T. J., et al. 1998, Nature, 395, 670

Garcia-Segura, G., Langer, N., & MacLow, M.-M. 1996, A&A, 316, 133

Gezari, S. et al. 2008, ApJ, 683, L131

Hammell, M. C., & Fesen, R. A. 2008, ApJS, 179, 195

Helder, E. A., & Vink, J. 2008, ApJ, 686, 1094

Hwang, U., & Laming, J. M. 2003, ApJ, 597, 362

Hwang, U. et al. 2004, ApJ, 615, L117

Keohane, J. W., Rudnick, L., & Anderson, M. C. 1996, ApJ, 466, 309

Krause, O., et al. 2008, Science, 320, 1195

Laming, J. M. 2001a, ApJ, 546, 1149

Laming, J. M. 2001b, ApJ, 563, 828

Laming, J. M., & Hwang, U. 2003, ApJ, 597, 347

Laming, J. M., Hwang, U., Radics, B., Lekli, G., & Takács, E. 2006, ApJ, 644, 260

Markert, T. H., Clark, G. W., Winkler, P. F., & Canizares, C. R. 1983, ApJ, 269, 134

Matzner, C. D., & McKee, C. F. 1999, ApJ, 510, 379

Mazzali, P., et al. 2006, Nature, 442, 1018

Patnaude, D., J., & Fesen, R. A. 2007, ApJ, 133, 147

Rest, A., et al. 2008, ApJ, 681, L81

Schawinski, K., et al. 2008, Science, 321, 223

Schure, K. M., Vink, J., Garcia-Segura, G., & Achterberg, A. 2008, ApJ, 686, 399

Soderberg, A., et al. 2006, Nature, 442, 1014

Soderberg, A., et al. 2008, Nature, 453, 469

Thorstensen, J. R., & Fesen, R. A. 2001, AJ, 122, 297

Troland, T.H., Crutcher, R. M., & Heiles, C. 1985, ApJ, 298, 808

Uchiyama, Y., & Aharonian, F. 2008, ApJ, 677, L105

Willingale, R., et al. 2002, A&A, 381, 1039

Woosley, S. E., Langer, N., & Weaver, T. A. 1993, ApJ, 411, 823

Young, P. A., Fryer, C. L., Hungerford, A., Arnett, D., Rockefeller, G., Timmes, F. X., Voit,
    B., Meakin, C., Eriksen, K. 2006, ApJ, 640, 891

Table 1.

Knot	χ^2	N_H	kT	$n_e t$	Si	Fe	kT_{Fe}	$n_e t_{Fe}$
A1	316.0, 1.43	1.45 (1.45-1.47)	1.25 (1.23-1.27)	0.62 (0.61-0.64)	0.73 (0.72-0.75)	0.05 (0.05-0.06)	68.80 (69.62-67.98)	0.00 (0.00-0.02)
A2	357.5, 1.54	1.53 (1.52-1.54)	1.14 (1.12-1.16)	0.53 (0.52-0.54)	0.90 (0.88-0.91)	0.05 (0.05-0.06)	1.64 (1.51-1.79)	38.39 (7.51-500.00)
A3	265.9, 1.01	1.36 (1.35-1.37)	2.62 (2.57-2.69)	0.57 (0.56-0.58)	0.47 (0.46-0.48)	0.06 (0.06-0.07)	2.67 (2.49-3.99)	2.51 (2.28-3.77)
A4	162.4, 0.76	1.38 (1.34-1.44)	1.25 (1.23-1.40)	0.58 (0.52-0.61)	0.53 (0.48-0.56)	0.07 (0.07-0.08)	5.13 (3.75-8.41)	1.03 (0.97-1.37)
A5	411.6, 1.60	1.64 (1.62-1.65)	1.37 (1.36-1.40)	0.44 (0.43-0.46)	0.70 (0.67-0.72)	0.01 (0.01-0.02)	0.92 (0.89-0.96)	310.04 (4.06-500.00)
A6	370.5, 1.17	1.52 (1.51-1.55)	1.74 (1.67-1.77)	0.55 (0.54-0.56)	0.15 (0.15-0.16)	0.06 (0.06-0.07)	2.28 (2.18-2.54)	2.87 (2.66-3.33)
A7	199.4, 0.68	1.24 (1.23-1.25)	1.60 (1.57-1.62)	1.20 (1.16-1.22)	0.11 (0.11-0.11)	0.02 (0.02-0.02)	1.76 (1.71-1.81)	0.29 (0.27-0.30)
A8	296.2, 1.22	1.38 (1.38-1.39)	1.65 (1.62-1.67)	0.52 (0.51-0.53)	0.59 (0.58-0.60)	0.13 (0.13-0.13)	1.81 (1.73-1.91)	11.28 (7.54-500.00)
A9	333.8, 1.28	1.41 (1.40-1.42)	2.00 (1.96-2.04)	0.56 (0.55-0.57)	0.60 (0.59-0.61)	0.12 (0.11-0.12)	1.89 (1.79-2.02)	28.78 (7.19-500.00)
A10	241.7, 0.97	1.16 (1.15-1.18)	1.57 (1.52-1.59)	1.26 (1.23-1.29)	0.45 (0.45-0.47)	0.04 (0.03-0.00)	4.76 (4.70-4.76)	0.01 (0.00-0.01)
B1	149.5, 0.77	1.36 (1.35-1.38)	1.62 (1.51-1.66)	0.52 (0.50-0.53)	0.82 (0.80-0.84)	0.21 (0.20-0.22)	1.82 (1.72-1.88)	4.57 (4.11-5.15)
B2	175.9, 0.87	1.36 (1.34-1.40)	1.49 (1.45-1.61)	0.66 (0.63-0.67)	0.66 (0.65-0.73)	0.23 (0.21-0.24)	3.35 (3.17-3.96)	1.54 (1.47-2.04)
B3	182.3, 0.88	1.10 (1.04-1.13)	0.92 (0.81-1.00)	2.55 (1.87-4.96)	0.70 (0.62-1.06)	0.08 (0.07-0.13)	2.11 (1.46-2.52)	41.63 (3.72-0.00)
B4	152.8, 0.74	1.47 (1.45-1.51)	1.31 (1.26-1.51)	1.28 (1.15-1.36)	0.69 (0.63-0.78)	0.20 (0.18-0.22)	0.15 (0.14-0.17)	0.12 (0.10-5.21)
B5	221.9, 0.96	1.37 (1.36-1.41)	1.18 (1.13-1.24)	1.64 (1.58-1.84)	0.56 (0.55-0.59)	0.18 (0.14-0.20)	1.39 (1.37-1.42)	0.18 (0.15-0.21)
B6	160.3, 0.75	1.16 (1.14-1.17)	1.18 (1.16-1.19)	2.60 (2.48-3.12)	0.41 (0.36-0.42)	0.11 (0.10-0.11)	2.34 (2.21-2.54)	3.88 (3.46-4.62)
B7	153.7, 0.69	1.56 (1.49-1.60)	1.39 (1.32-1.48)	2.19 (2.00-2.48)	0.41 (0.40-0.45)	0.31 (0.28-0.36)	1.36 (0.89-1.71)	0.15 (0.10-0.21)
B8	168.4, 0.72	1.06 (0.99-1.10)	1.90 (1.63-2.07)	1.86 (1.81-2.01)	0.40 (0.39-0.42)	0.16 (0.15-0.19)	79.90 (0.00-53.58)	1.02 (0.93-1.09)
B9	195.8, 0.94	1.09 (1.07-1.13)	0.95 (0.94-0.97)	77.49 (17.30-500.00)	0.50 (0.47-0.52)	0.07 (0.07-0.08)	2.05 (1.96-2.18)	5.57 (5.06-6.31)
B10	140.3, 0.68	1.58 (1.53-1.62)	1.47 (1.42-1.82)	2.63 (1.37-2.90)	0.60 (0.51-0.63)	0.62 (0.52-0.67)	0.64 (0.59-0.69)	20.00 (1.75-500.00)
B11	200.0, 0.85	1.40 (1.38-1.43)	1.03 (1.03-1.04)	50.00 (22.60-500.00)	0.81 (0.66-0.84)	0.42 (0.38-0.44)	2.50 (2.40-2.71)	2.19 (2.03-2.37)
B12	204.8, 1.00	1.13 (1.12-1.18)	1.01 (0.99-1.01)	30.00 (18.40-500.00)	0.37 (0.34-0.41)	0.14 (0.14-0.15)	2.51 (2.43-2.97)	2.30 (2.20-2.56)
C1	181.7, 0.82	1.51 (1.50-1.54)	1.40 (1.37-1.48)	0.56 (0.54-0.58)	0.62 (0.59-0.66)	0.14 (0.13-0.15)	1.52 (1.46-1.59)	34.09 (10.46-500.00)
C2	184.8, 0.88	1.14 (1.13-1.16)	1.04 (1.02-1.05)	2.50 (2.35-3.26)	0.46 (0.45-0.51)	0.05 (0.04-0.05)	2.34 (2.26-2.45)	4.46 (4.04-12.96)
C3	196.3, 0.86	1.17 (1.16-1.18)	1.02 (1.00-1.07)	4.93 (4.61-5.32)	0.43 (0.42-0.44)	0.06 (0.06-0.07)	2.15 (1.18-2.24)	5.02 (4.59-5.64)
C4	208.2, 0.91	0.98 (0.96-1.02)	1.18 (1.15-1.21)	1.75 (1.64-2.10)	0.38 (0.37-0.41)	0.03 (0.03-0.03)	2.36 (2.28-2.47)	5.89 (5.17-7.65)
C5	282.4, 1.10	1.81 (1.79-1.83)	1.30 (1.28-1.38)	1.83 (1.60-1.89)	0.35 (0.34-0.36)	0.17 (0.16-0.18)	0.68 (0.62-0.80)	0.43 (0.37-0.53)
C6	274.9, 1.16	1.16 (1.15-1.18)	0.99 (0.98-1.00)	6.32 (5.84-6.93)	0.37 (0.36-0.41)	0.03 (0.03-0.04)	2.61 (2.54-2.71)	3.60 (3.43-3.83)
C7	223.4, 0.98	1.99 (1.89-2.01)	1.33 (1.26-1.40)	1.60 (1.53-1.97)	0.55 (0.50-0.62)	0.24 (0.15-0.26)	0.54 (0.50-0.64)	1.56 (0.61-500.00)
C8	268.7, 1.16	1.83 (1.82-1.85)	0.89 (0.88-0.90)	93.83 (25.40-500.00)	0.93 (0.90-1.12)	0.58 (0.46-0.60)	2.30 (2.23-2.38)	2.67 (2.53-2.82)
C9	240.9, 0.97	0.77 (0.75-0.78)	3.42 (3.17-3.51)	1.33 (1.31-1.55)	0.46 (0.44-0.54)	0.20 (0.18-0.21)	54.63 (49.60-58.99)	0.95 (0.89-1.00)
C10	302.3, 1.15	0.88 (0.86-0.89)	1.55 (1.48-1.61)	6.77 (5.70-10.00)	0.54 (0.52-0.55)	0.18 (0.18-0.19)	52.28 (40.68-57.52)	0.95 (0.90-1.02)
C11	174.9, 0.85	0.98 (0.93-1.02)	0.75 (0.73-0.76)	15.64 (11.54-500.00)	0.54 (0.52-0.64)	0.07 (0.06-0.08)	10.15 (10.08-10.31)	0.86 (0.80-0.87)
D1	380.8, 1.40	1.21 (1.18-1.22)	1.17 (1.13-1.21)	1.15 (1.06-1.24)	0.44 (0.43-0.45)	0.03 (0.03-0.03)	2.14 (2.08-2.22)	10.36 (7.69-500.00)

Table 1—Continued

Knot	χ^2	N_H	kT	$n_e t$	Si	Fe	kT_{Fe}	$n_e t_{Fe}$
D2	342.4, 1.28	1.46 (1.44-1.47)	1.63 (1.60-1.72)	0.61 (0.56-0.74)	0.54 (0.52-0.56)	0.08 (0.07-0.08)	1.86 (1.83-1.93)	19.99 (8.93-500.00)
D3	850.3, 2.39	1.56 (1.55-1.57)	2.84 (2.82-2.87)	0.63 (0.63-0.64)	0.28 (0.27-0.28)	0.04 (0.04-0.04)	2.08 (2.03-2.24)	7.90 (6.14-500.00)
D4	335.6, 1.15	1.06 (1.05-1.07)	1.65 (1.57-1.72)	1.75 (1.71-1.86)	0.33 (0.32-0.33)	0.03 (0.03-0.03)	2.62 (2.52-3.35)	4.88 (4.38-5.71)
D5	658.8, 1.65	1.23 (1.22-1.24)	2.79 (2.74-2.79)	1.26 (1.24-1.26)	0.28 (0.28-0.28)	0.05 (0.05-0.05)	34.02 (26.38-40.67)	0.97 (0.92-1.03)
D6	251.9, 0.87	1.09 (1.08-1.11)	2.74 (2.71-2.95)	1.56 (1.53-1.59)	0.38 (0.37-0.39)	0.06 (0.06-0.06)	7.19 (4.54-9.92)	29.95 (2.56-500.00)
D7	249.9, 1.00	1.11 (1.09-1.14)	1.29 (1.21-1.39)	6.48 (4.17-10.78)	0.49 (0.44-0.55)	0.03 (0.02-0.04)	3.46 (3.32-3.61)	2.37 (2.26-4.64)
D8	204.3, 0.90	1.16 (1.11-1.19)	0.89 (0.88-0.90)	12.70 (10.38-500.00)	0.69 (0.64-0.74)	0.04 (0.04-0.06)	2.12 (1.79-2.19)	5.19 (4.90-8.52)
D9	168.2, 0.82	1.08 (1.06-1.09)	0.91 (0.90-0.92)	12.72 (10.47-500.00)	0.60 (0.58-0.62)	0.05 (0.04-0.05)	2.37 (2.32-2.43)	3.81 (3.64-4.00)
D10	245.4, 0.84	1.22 (1.21-1.24)	2.10 (2.07-2.12)	1.21 (1.19-1.24)	0.29 (0.28-0.29)	0.04 (0.04-0.04)	2.87 (2.54-3.32)	40.00 (4.57-500.00)
E1	579.9, 1.67	1.18 (1.16-1.20)	1.28 (1.26-1.31)	3.40 (3.10-3.69)	0.39 (0.37-0.40)	0.07 (0.06-0.08)	5.42 (5.07-5.51)	1.34 (1.32-1.39)
E2	401.9, 1.31	1.33 (1.30-1.34)	1.21 (1.13-1.26)	5.67 (5.34-12.86)	0.61 (0.59-0.66)	0.24 (0.20-0.27)	3.21 (3.14-3.29)	1.93 (1.89-2.03)
E3	253.6, 0.96	1.10 (1.05-1.16)	1.28 (1.23-1.35)	5.00 (3.51-6.85)	0.48 (0.40-0.53)	0.10 (0.09-0.15)	5.22 (4.29-5.51)	1.21 (1.19-1.35)
E4	192.9, 0.77	1.15 (1.12-1.20)	1.27 (1.23-1.29)	5.39 (4.54-5.68)	0.58 (0.54-0.65)	0.17 (0.16-0.22)	5.37 (4.36-5.53)	1.12 (1.10-1.16)
E5	174.8, 0.76	1.63 (1.61-1.64)	1.51 (1.47-1.52)	2.81 (2.69-2.91)	1.21 (1.18-1.40)	1.88 (1.77-2.49)	0.63 (0.61-0.67)	35.38 (1.47-500.00)
E6	504.3, 1.51	1.25 (1.23-1.28)	1.22 (1.19-1.25)	3.39 (3.23-3.52)	0.40 (0.40-0.41)	0.10 (0.09-0.10)	3.35 (3.20-3.62)	2.44 (2.32-2.50)
E7	941.0, 2.54	1.13 (1.12-1.14)	1.28 (1.28-1.32)	2.24 (2.21-2.41)	0.32 (0.31-0.33)	0.06 (0.05-0.06)	3.21 (3.14-3.26)	3.54 (3.42-3.66)
F1	477.4, 1.63	1.07 (1.06-1.08)	1.02 (1.01-1.02)	4.96 (4.65-5.13)	0.42 (0.41-0.43)	0.05 (0.05-0.06)	2.47 (2.40-2.54)	5.77 (5.21-6.83)
F2	306.9, 1.25	1.09 (1.08-1.10)	0.89 (0.88-0.89)	11.47 (10.18-13.27)	0.58 (0.55-0.59)	0.09 (0.08-0.09)	2.28 (2.17-2.36)	7.24 (6.01-12.29)
F3	191.6, 0.84	0.99 (0.98-1.03)	1.02 (1.01-1.05)	3.25 (3.00-3.40)	0.49 (0.43-0.60)	0.09 (0.07-0.09)	2.48 (2.30-2.71)	43.54 (5.89-500.00)
F4	129.0, 0.61	1.03 (1.00-1.04)	1.05 (1.04-1.06)	3.57 (2.56-3.76)	0.52 (0.51-0.54)	0.10 (0.09-0.10)	1.87 (1.83-1.99)	7.60 (6.18-500.00)
F5	186.4, 0.82	1.01 (0.99-1.04)	1.14 (1.10-1.16)	2.64 (2.47-2.80)	0.31 (0.28-0.33)	0.07 (0.06-0.07)	3.11 (2.52-3.69)	2.31 (1.84-5.14)
G1	430.6, 1.66	1.49 (1.48-1.50)	1.28 (1.27-1.29)	0.70 (0.69-0.71)	0.44 (0.43-0.45)	0.23 (0.22-0.23)	1.88 (1.80-2.00)	68.41 (9.04-500.00)
G2	244.3, 1.08	1.35 (1.34-1.36)	1.20 (1.14-1.27)	1.56 (1.48-1.62)	0.39 (0.36-0.40)	0.18 (0.15-0.18)	1.22 (1.15-1.28)	0.23 (0.19-0.27)
G3	162.2, 0.71	0.93 (0.92-0.94)	1.02 (0.95-1.06)	2.78 (2.61-2.95)	0.48 (0.47-0.52)	0.07 (0.06-0.07)	10.86 (10.84-12.74)	0.43 (0.40-0.45)
G4	295.1, 1.31	1.03 (1.02-1.05)	0.75 (0.75-0.76)	17.92 (13.49-34.41)	0.70 (0.54-0.71)	0.09 (0.08-0.09)	2.26 (2.07-2.37)	68.41 (7.48-500.00)
G5	460.8, 1.68	1.50 (1.49-1.51)	1.59 (1.56-1.60)	0.51 (0.51-0.52)	0.44 (0.43-0.44)	0.22 (0.21-0.22)	2.06 (2.00-2.13)	3.35 (3.14-3.56)
H1	340.9, 0.97	1.91 (1.90-1.92)	2.15 (2.12-2.23)	0.62 (0.61-0.64)	0.08 (0.08-0.09)	0.04 (0.04-0.04)	0.59 (0.58-0.59)	75.18 (26.20-500.00)
H2	287.0, 1.07	1.75 (1.74-1.77)	1.53 (1.48-1.59)	0.42 (0.41-0.43)	0.40 (0.39-0.41)	0.17 (0.16-0.17)	1.58 (1.41-1.77)	50.18 (5.75-500.00)
H3	339.4, 1.29	1.70 (1.69-1.72)	1.48 (1.45-1.50)	0.47 (0.46-0.47)	0.48 (0.48-0.49)	0.14 (0.13-0.14)	1.68 (1.59-1.78)	50.05 (8.09-500.00)
H4	333.1, 1.21	1.70 (1.69-1.71)	1.55 (1.52-1.59)	0.57 (0.55-0.58)	0.22 (0.22-0.22)	0.12 (0.12-0.12)	2.76 (2.61-2.92)	1.57 (1.46-1.67)
H5	532.9, 1.93	1.53 (1.52-1.55)	0.99 (0.98-1.00)	1.16 (1.13-1.18)	0.20 (0.20-0.21)	0.09 (0.09-0.09)	2.73 (2.63-2.84)	1.63 (1.55-1.72)
H6	323.6, 1.16	1.45 (1.40-1.48)	1.12 (1.07-1.16)	1.85 (1.68-2.12)	0.17 (0.17-0.17)	0.06 (0.04-0.08)	1.36 (1.32-1.41)	0.22 (0.20-0.23)
J1	438.1, 1.02	1.83 (1.82-1.86)	2.57 (2.49-2.61)	0.79 (0.77-0.80)	0.10 (0.09-0.10)	0.01 (0.01-0.01)	3.57 (2.72-3.93)	1.95 (1.67-2.90)
J2	537.0, 1.25	2.83 (2.82-2.85)	2.31 (2.25-2.33)	1.14 (1.13-1.18)	0.21 (0.20-0.22)	0.11 (0.09-0.11)	1.86 (1.79-1.93)	40.00 (7.53-500.00)

Table 1—Continued

Knot	χ^2	N_H	kT	$n_e t$	Si	Fe	kT_{Fe}	$n_e t_{Fe}$
J3	499.2, 1.13	1.91 (1.90-1.96)	2.64 (2.61-2.66)	0.95 (0.93-0.96)	0.10 (0.10-0.10)	0.00 (0.00-0.00)	3.59 (3.32-4.04)	5.20 (4.49-0.00)
J4	347.9, 0.90	1.71 (1.68-1.73)	1.85 (1.84-1.87)	1.52 (1.50-1.55)	0.14 (0.14-0.14)	0.00 (0.00-0.01)	10.85 (9.73-15.12)	1.63 (1.43-1.91)
J5	440.6, 1.16	1.73 (1.68-1.79)	1.66 (1.63-1.72)	1.85 (1.77-1.93)	0.13 (0.13-0.14)	0.00 (0.00-0.00)	10.68 (10.65-10.77)	0.71 (0.68-0.75)
J6	550.2, 1.47	3.24 (3.23-3.25)	1.12 (1.12-1.13)	4.85 (4.70-5.09)	2.68 (2.65-2.72)	3.90 (3.84-8.26)	10.85 (10.82-12.92)	0.53 (0.52-0.56)
J7	756.6, 2.04	3.23 (3.22-3.25)	1.14 (1.13-1.15)	2.30 (2.25-2.33)	0.72 (0.71-0.83)	1.26 (1.23-1.28)	4.29 (4.06-4.46)	1.08 (1.04-1.12)
J8	654.7, 1.69	3.32 (3.30-3.33)	1.07 (1.07-1.08)	6.22 (6.01-6.45)	1.61 (1.60-1.64)	1.74 (1.70-1.78)	10.86 (10.83-11.87)	0.51 (0.50-0.52)
K1	281.8, 0.75	1.97 (1.94-1.99)	0.82 (0.81-0.83)	96.01 (18.49-500.00)	0.09 (0.09-0.10)	0.09 (0.07-0.09)	10.85 (10.85-10.90)	0.03 (0.02-0.03)
K2	204.2, 0.61	1.54 (1.50-1.56)	1.43 (1.37-1.45)	1.51 (1.44-1.57)	0.06 (0.06-0.06)	0.02 (0.02-0.02)	20.61 (20.09-21.08)	0.47 (0.45-0.49)
K3	288.5, 0.95	2.06 (2.05-2.08)	1.24 (1.21-1.26)	1.84 (1.76-1.96)	0.10 (0.09-0.10)	0.06 (0.05-0.06)	1.37 (1.33-1.39)	0.17 (0.14-0.20)
K4	300.3, 0.92	1.53 (1.52-1.54)	1.48 (1.46-1.50)	1.59 (1.55-1.62)	0.09 (0.09-0.09)	0.00 (0.00-0.00)	4.44 (4.11-4.67)	1.50 (1.41-1.56)
K5	332.6, 1.08	1.59 (1.55-1.60)	1.27 (1.24-1.29)	1.51 (1.45-1.56)	0.08 (0.08-0.09)	0.01 (0.01-0.02)	3.17 (3.00-3.40)	2.23 (2.08-3.28)
L1	241.2, 0.79	1.63 (1.62-1.65)	1.62 (1.57-1.65)	1.03 (1.00-1.09)	0.04 (0.03-0.04)	0.02 (0.02-0.02)	0.14 (0.14-0.16)	0.26 (0.26-0.26)
L2	301.5, 1.05	1.54 (1.53-1.55)	1.39 (1.36-1.41)	0.70 (0.69-0.72)	0.07 (0.06-0.07)	0.08 (0.08-0.09)	2.77 (1.57-2.95)	2.08 (1.94-2.24)
L3	584.6, 1.78	1.46 (1.45-1.47)	2.00 (1.98-2.03)	0.55 (0.55-0.56)	0.14 (0.14-0.14)	0.08 (0.08-0.08)	2.75 (2.68-2.85)	2.25 (2.14-3.68)
L4	412.4, 1.31	1.55 (1.54-1.56)	2.55 (2.47-2.61)	0.48 (0.47-0.49)	0.20 (0.19-0.20)	0.08 (0.07-0.08)	1.88 (1.77-1.95)	40.00 (7.95-500.00)
L5	424.9, 1.18	1.60 (1.59-1.61)	2.73 (2.66-2.79)	0.50 (0.49-0.51)	0.10 (0.10-0.10)	0.05 (0.05-0.05)	2.18 (2.12-2.24)	3.98 (3.63-4.34)
L6	400.6, 1.21	1.49 (1.48-1.50)	2.53 (2.50-2.58)	0.60 (0.59-0.61)	0.18 (0.17-0.18)	0.09 (0.09-0.09)	4.31 (4.04-4.57)	1.41 (1.34-1.47)
M1	495.3, 1.51	1.32 (1.31-1.33)	2.75 (2.68-2.79)	0.61 (0.61-0.62)	0.20 (0.20-0.21)	0.08 (0.08-0.08)	2.50 (2.41-2.57)	3.70 (3.47-3.95)
M2	543.3, 1.81	1.43 (1.42-1.44)	2.73 (2.69-2.77)	0.44 (0.43-0.44)	0.30 (0.30-0.31)	0.09 (0.09-0.10)	2.04 (1.98-2.10)	6.65 (5.84-8.14)
M3	409.8, 1.35	1.42 (1.41-1.43)	2.88 (2.80-2.92)	0.46 (0.45-0.46)	0.25 (0.24-0.25)	0.08 (0.07-0.08)	2.19 (2.12-2.30)	3.92 (3.49-6.08)
M4	373.7, 1.33	1.34 (1.33-1.35)	2.92 (2.87-3.00)	0.48 (0.47-0.49)	0.35 (0.34-0.36)	0.12 (0.11-0.12)	2.37 (2.27-2.50)	3.66 (3.41-4.04)
M5	387.4, 1.40	1.29 (1.29-1.31)	2.57 (2.52-2.63)	0.52 (0.52-0.53)	0.36 (0.36-0.37)	0.13 (0.12-0.13)	2.18 (2.08-2.32)	56.02 (6.47-500.00)
M6	381.8, 1.34	1.21 (1.21-1.23)	2.15 (2.10-2.17)	0.84 (0.77-0.87)	0.34 (0.33-0.35)	0.08 (0.07-0.08)	0.61 (0.60-0.62)	60.00 (2.41-500.00)
M7	182.7, 0.69	1.09 (1.04-1.13)	1.54 (1.46-1.66)	1.99 (1.72-2.09)	0.14 (0.13-0.14)	0.04 (0.04-0.04)	1.92 (1.40-2.09)	0.27 (0.26-0.30)
N1	807.4, 2.21	1.25 (1.24-1.25)	2.41 (2.38-2.43)	0.55 (0.54-0.55)	0.22 (0.21-0.22)	0.07 (0.07-0.08)	1.93 (1.91-1.98)	68.41 (8.95-500.00)
N2	670.3, 2.26	1.42 (1.41-1.42)	2.16 (2.15-2.19)	0.36 (0.36-0.37)	0.46 (0.45-0.46)	0.08 (0.07-0.08)	1.78 (1.72-1.86)	34.84 (10.38-500.00)
N3	483.4, 1.67	1.43 (1.43-1.44)	2.15 (2.12-2.16)	0.49 (0.49-0.50)	0.42 (0.42-0.43)	0.09 (0.08-0.09)	2.34 (2.23-2.57)	3.62 (3.31-4.59)
N4	389.4, 1.36	1.20 (1.20-1.21)	2.01 (1.98-2.04)	0.66 (0.66-0.67)	0.38 (0.37-0.38)	0.08 (0.08-0.08)	2.10 (1.98-2.21)	30.00 (6.75-500.00)
N5	359.4, 1.40	1.24 (1.23-1.26)	1.81 (1.78-1.84)	0.66 (0.64-0.67)	0.50 (0.49-0.51)	0.06 (0.05-0.06)	2.10 (1.82-2.28)	49.18 (6.30-500.00)

Table 2.   SNR Models

Bubble size (pc)	blast wave radius (pc)	blast wave speed (km s^{-1})	SNR age (yrs)
0.0	2.37	5072	325
0.0	2.5	4930	350
0.1	2.5	4791	339
0.2	2.5	5007	331
0.3	2.5	5044	324

Table 3.   Abundance sets by mass

knot	O	Ne	Mg	Si	S	Fe
M4	0.941	0.006		0.017		0.022
M6	0.9092	0.0321	0.004	0.0306		0.0281
K4	0.783	0.187				0.030
K10	0.9260	0.0485				0.0112
G3	0.9185			0.0408		0.0407
C10	0.711	0.1413		0.0875		0.0602
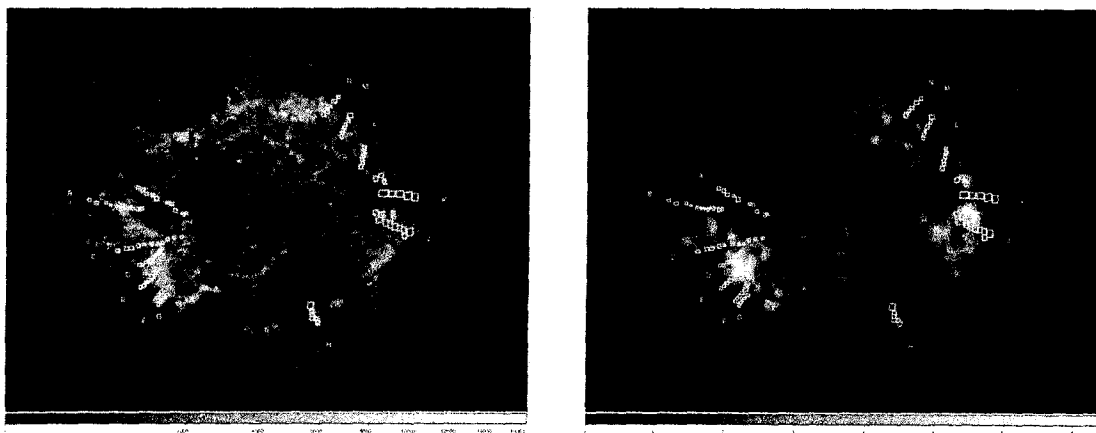
Fig. 1.— (Left:) Radial series of knots labelled by letter overlaid on the Chandra ACIS broadband image of Cas A. The regions are numbered from the inside out towards the remnant edge. (Right:) The same regions overlaid on the smoothed 8-15 keV XMM-Newton PN image from 2000.
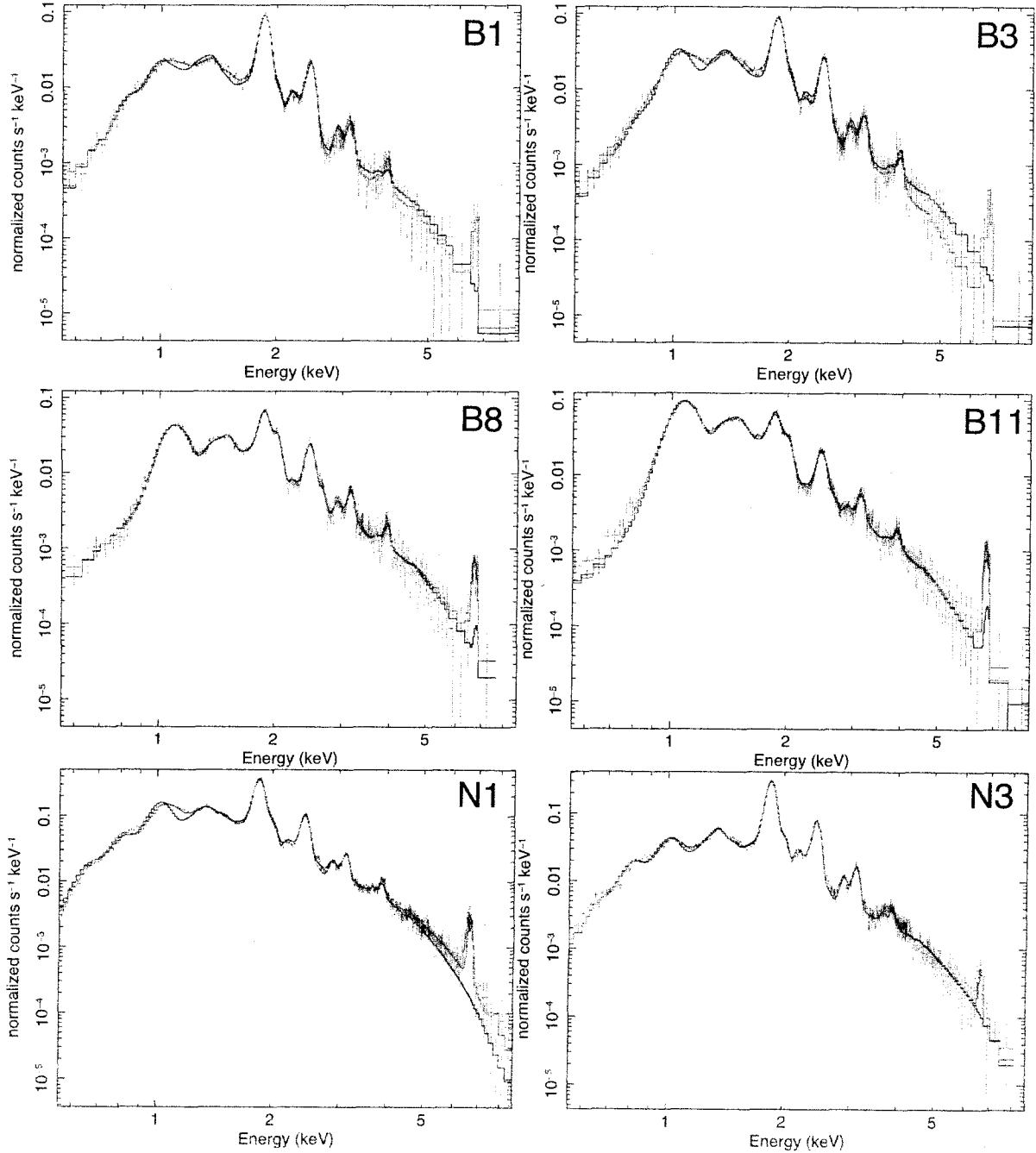
Fig. 2.— Selected spectra from the B and N series showing both single (black) and two (red) NEI models as described in the text.
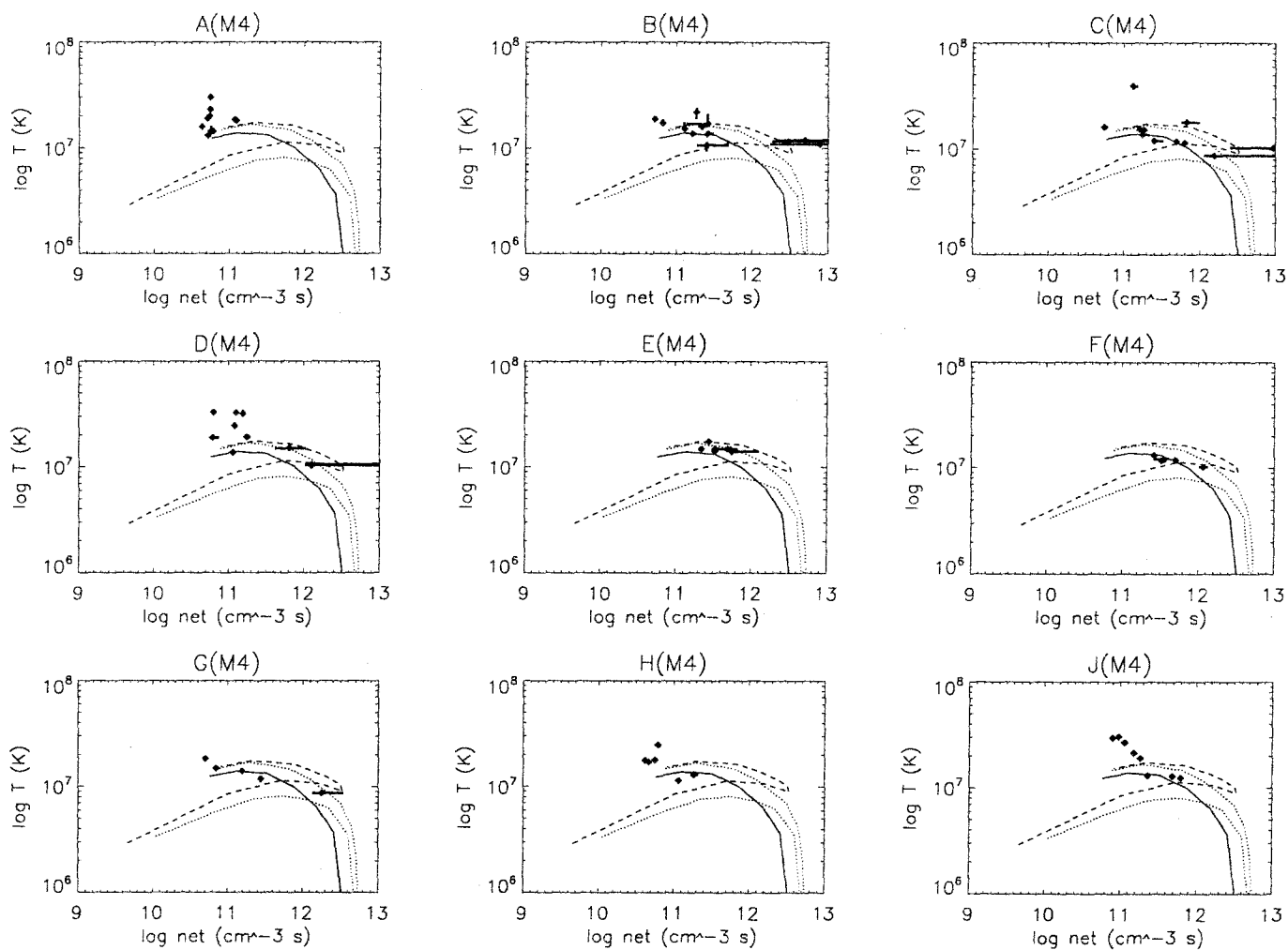
Fig. 3.— Plots of measured temperature and ionization age for each of the series of knots pictured in Figure 1 for the M4 set of abundances in Table 2. The curves show models for the evolution of temperature and ionization age in a circumstellar wind with a central bubble of size 0, 0.2, and 0.3 pc respectively (bottom to top: solid, dotted, and dashed). For series N, models for the K10 and C10 sets of abundances are also shown, to illustrate the effect of the range of abundances considered in the calculated models.
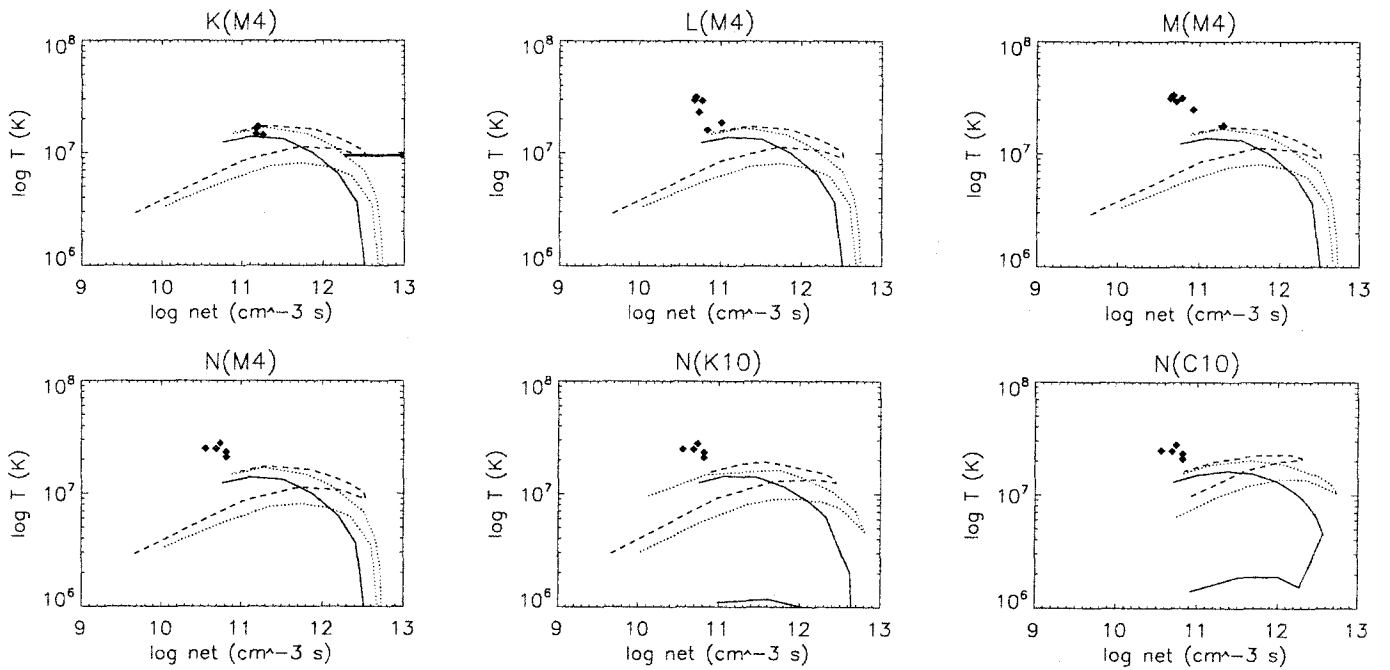
Fig. 3.— continued